Supporting Information

Atmospheric Pressure Plasma Jet Induced Ultrafast Construction of Ultra-Thin Non-stoichiometric Nickel Oxide Layer with Mixed Ni^{3+}/Ni^{2+} Ions and Rich Oxygen Defects as An Efficient Electrocatalyst for Oxygen Evolution Reaction

Baoan Zhang[†], Xiaonan Shang[†], Zhongqing Jiang[†,*], Changsheng Song[†,*], Thandavarayan Maiyalagan[§], Zhong-Jie Jiang[‡,*]

[†] Key Laboratory of Optical Field Manipulation of Zhejiang Province, Department of Physics, Zhejiang Sci-Tech University, Hangzhou 310018, P. R. China.
[‡] Guangdong Engineering and Technology Research Center for Surface Chemistry of Energy Materials & Guangzhou Key Laboratory for Surface Chemistry of Energy Materials, New Energy Research Institute, College of Environment and Energy, South China University of Technology, Guangzhou 510006, P. R. China.
[§] Electrochemical Energy Laboratory, Department of Chemistry, SRM Institute of Science and Technology, SRM Nagar, Kattankulathur 603203, India.
***Corresponding authors**
E-mail: zhongqingjiang@hotmail.com or zhongqingjiang@zstu.edu.cn (Z. Jiang).
E-mail: cssong@zstu.edu.cn (C. Song).
E-mail: eszjiang@scut.edu.cn (Z.-J. Jiang).

Experimental

1.1 Chemicals

Nickel foam (NF, thickness: 1.6 mm) was purchased from Changsha Lyrun Materials Co., Ltd. Platinum nanoparticles supported on graphitized carbon (20 wt% Pt/C) was purchased from Sigma-Aldrich. All of the chemicals used in the synthesis process were analytical grade and were used without further treatment.

1.2 Preparation of ultra-thin Ni_xO_y nanosheets on Ni foam (APPJ-Ni_xO_y/NF)

In a general synthesis, a piece of nickel foam (NF) was first washed with 4 M diluted hydrochloric acid, absolute ethanol and deionized water few times in sequence to remove the oil and nickel oxide layers on the surface, and dried in a vacuum oven for 24 h. The cleaned NF was then cut into 1 cm × 1 cm squares and treated with an atmospheric pressure nonequilibrium oxygen plasma jet for the predesigned time. The process of generating oxygen plasma jet was conducted by a high-frequency generator with a frequency of 20 KHz (PG-1000ZD, Nanjing Suman Plasma Technology Co., Ltd). In order to optimize the thickness of the Ni_xO_y layer and the OER performance of the APPJ-Ni_xO_y/NFs, we prepared APPJ-Ni_xO_y/NFs materials with different plasma

treatment time of 1 min, 3 min, 5 min and 7 min, and named them APPJ-Ni_xO_y/NF-1, APPJ-Ni_xO_y/NF-3, APPJ-Ni_xO_y/NF-5 and APPJ-Ni_xO_y/NF-7, respectively. The condition for the oxygen plasma jet was high-purity oxygen of about 0.1 MPa, discharge power of 300 W, and gas flow rate of about 0.4 L min^{-1}. The whole process is carried out at room temperature.

1.3 Characterization

The phase composition of the as-prepared samples was determined by X-ray diffraction (XRD, Bruker D8 diffractometer) using Cu Kα (λ = 1.5406 Å) radiation at 40 KV and 40 mA. The micromorphology of the samples was characterized by scanning electron microscopy (FESEM, Hitachi S-4800) and transmission electron microscopy (TEM, JEM-2100). X-ray photoelectron spectroscopy (XPS) measurement was performed with a Thermo Fischer ESCALAB 250Xi spectrophotometer. Optical emission spectroscopy (OES) was provided by a handheld spectrometer (Ocean Optics Corporation, USA) with a spectral resolution of 0.4 nm.

1.4 Electrochemical activity measurement

Electrochemical measurements were conducted on an electrochemical workstation (CHI 760E, CH Instruments Inc., China) using a three-electrode mode in 1.0 M KOH solution (pH = ∼13). The reference and counter electrodes were saturated calomel electrode (SCE, saturated KCl solution as electrolyte) and platinum wire, respectively. The NF and the APPJ-Ni_xO_y/NFs electrodes were directly used as the anodes for electrochemical characterizations.

Linear sweep voltammetry (LSV) was performed at a scan rate of 5 mV s^{-1} between 0.191 V and 0.791 V (vs. SCE). Tafel slopes were calculated based on the LSV curves by plotting overpotential (vs. the RHE) against log (current density). All curve tests are the results of repeated test after stabilization. The potential reported was converted with respect to a reversible hydrogen electrode (RHE) according to the pH value: $E_{RHE} = E_{SCE} + 0.242 + 0.059pH$. Unless specifically mentioned, all polarization curves were corrected for the iR compensation. The iR internal resistance correction was done using the equation : E_{RHE} compensation = E_{RHE}-iR. The Tafel curve was conducted in the potential range where there was no obvious Faraday current according to the formula: E = a + b log j. (where b is the Tafel slope, reflecting the catalytic mechanism of the material). EIS measurements were carried out at 1.56 V vs RHE over a frequency range from 10^5 to 0.01 Hz with a 5 mV AC dither. Chronopotentiometry tests were performed at the current density of 10 mA cm^{-2}. The stability evaluation was performed by measuring the CVs with a sweep rate of 50 mV s^{-1} for 1000 cycles. The overpotential (ŋ) was calculated using the following equation: $ŋ = E_{RHE}$-1.23 V.

The overall water splitting tests were conducted in a two-electrode system with the NF and the APPJ-Ni_xO_y/NF-5 electrodes as anodes and commercial Pt/C as cathode on the CHI760E electrochemical station. The LSV curves were recorded in 1.0 M KOH with a scan rate of 2 mV s^{-1}. The stability of the catalyst electrodes was assessed by chronopotentiometry at the constant current of 10 mA cm^{-2}, 30 mA cm^{-2}, 50 mA cm^{-2}, respectively. The final oxygen production at the current density of 10 mA cm^{-2} was

collected by a soap bubble flowmeter.

1.5 Electrochemical active surface area (ECSA)

The active surface area of the catalyst was estimated by calculating the electrochemical double-layer capacitance of the catalyst. Specifically, for a standard with an actual surface area of 1 cm^2, the specific capacitance value can be used to further convert C_{dl} into ECSA. Generally, the specific capacitance of a flat surface is usually between 0.02-0.06 mF cm^{-2}. It is worth noting that using nickel foam as a support has a much larger capacitance value than a flat surface. Therefore, nickel foam is the standard here. The ECSA of each catalyst can be calculated according to the following formula[1]:

$$A_{ECSA} = \frac{C_{dl} - \text{catalyst}(\text{mF cm}^{-2})}{C_{dl} - \text{Ni foam}(\text{mF cm}^{-2})\text{per ECSA cm}^2}$$

Taking the APPJ-Ni_xO_y/NF-5 as an example, in the OER, the A_{ECSA} of APPJ-Ni_xO_y/NF-5 can be calculated as:

$$A_{ECSA}^{NiO/NF-5} = \frac{1.99 \text{ mF cm}^{-2}}{1.01 \text{ mF cm}^{-2} \text{ per cm}^2_{ECSA}} = 1.97 \text{ cm}^2_{ECSA}$$

The calculated ECSA was further used in the calculation of turnover frequency.

1.6 Turnover frequency (TOF) calculations

The TOF values were calculated according to the following formula:

$$\text{TOF} = \frac{\#\text{ total oxygen turn overs /geometric area}(\text{cm}^2)}{\#\text{ surface active sites/geometric area}(\text{cm}^2)}$$

The number of the total oxygen can be calculated based on the current density (J, IR-corrected) according to:

$$\#\ O_2 = J\frac{\text{mA}}{\text{cm}^2} \cdot \frac{1\text{C s}^{-1}}{1000\text{ mA}} \cdot \frac{1\text{ mol e}^-}{96495.3\text{ C}} \cdot \frac{1\text{ mol }O_2}{4\text{ mol e}^-} \cdot \frac{6.022 \times 10^{23}\ O_2\text{ molecules}}{1\text{ mol }O_2}$$
$$= 1.56 \times 10^{15} \frac{O_2\ \text{s}^{-1}}{\text{cm}^2} \text{per} \frac{\text{mA}}{\text{cm}^2}$$

Note that the nature of the surface active sites is not yet understood and the exact number of oxygen binding sites is not known, we thus estimated the number of the active sites as the total number of the surface sites (including metal Ni and oxygen atoms-according to our calculations, oxygen atoms also act as active sites) from the roughness factor together with the unit cell of the catalysts, which may underestimate the real TOF. Taking NiO (see figure below for the crystal structure) as an example, the surface active sites per real surface area can be calculated as follows:

$$\#\text{ Surface sites} = \left(\frac{8\text{ atoms per unit cell}}{71.84\text{ Å}^3\text{ per unit cell}}\right)^{\frac{2}{3}} = 2.314 \times 10^{15}\text{ atoms /cm}^2\text{ real surface area}$$

Similarly, the number of surface sites for Ni is calculated as 1.458×10^{15} atoms per cm^2 real surface area.

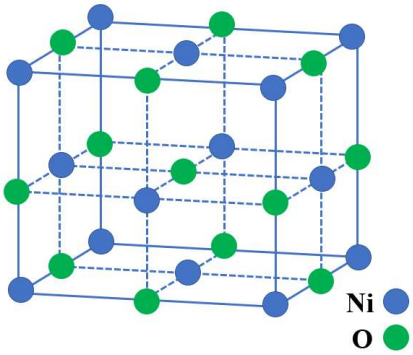

NiO unit cell contains 4 Ni and 4 O atoms.
Unit cell volume is 71.84 Å^3.

Finally, the TOF can be calculated as:

$$\mathrm{TOF} = \frac{1.56 \times 10^{15} \frac{\mathrm{O_2\ s^{-1}}}{\mathrm{cm^2}} \mathrm{per}\ \frac{\mathrm{mA}}{\mathrm{cm^2}} \times \mathrm{J}}{\#\ \text{surface active sites} \times \mathrm{A_{ECSA}}}$$

1.7 Computational methodology

The DFT calculations have been performed within the framework of density functional theory (DFT) as implemented by the Vienna an initio Simulation Package (VASP).[2-3] The exchange-correlation energy was treated in the generalized-gradient approximation (GGA) using Perdew-Burke-Ernzerhof PBE method[4]. The nano-model was constructed on the z direction of **Ni (Ni_{24}), Ni ($Ni_{20}O$)** with 16 Å vacuum. The cutoff energy of plane wave was chosen at 400 eV. For the structure optimizations, 6×6×1 Monkhorst-Pack (MP) grids were used. The changes in total energies between two successive iteration steps were less than 10^{-5} eV, and all the Hellmann-Feynman force acting on each atom was lower than 0.01 eV /Å. The dipole correction was not used in the calculation. The adsorption free energies of O, *OH and* OOH on all structures were calculated by the formula: $\Delta G = \Delta E + \Delta ZPE - T\Delta S$, where ΔE, ΔZPE, ΔS are the binding energy, zero point energy change and entropy change of H adsorption reaction, respectively. Herein, a solvation correction with energy equals to -0.22 eV is applied to only ΔE_{*OH} and ΔE_{*OOH} since water molecule could solvate *OH and *OOH moieties with hydrogen bond, whereas the hydrogen bond is absent for *O. For the OER intermediates, the adsorption Gibbs free energies are expressed by Ref. 5.

It is widely known that the OER is typical reversible reaction. It involves the four-electron transfer processes and elementary reactions pathways are displayed as following equations:

$$OH^- \xrightarrow{\Delta G1} *OH + e^- \quad (1)$$

$$*OH + OH^- \xrightarrow{\Delta G2} *O + H_2O + e^- \quad (2)$$

$$*O + OH^- \xrightarrow{\Delta G3} *OOH + e^- \quad (3)$$

$$*OOH + OH^- \xrightarrow{\Delta G4} O_2 + H_2O + e^- \quad (4)$$

where the "*" stand for the active adsorption site on catalysts.

According to the thermodynamics of OER, all the reaction steps are endothermic. The process with the largest endothermic process is the rate-determining step (RDS). The sample with the smallest U_L(OER) value has the highest OER catalytic activity, as described in the following equation:

$$U_L(\mathrm{OER}) = Max_i[\Delta G_i]/\mathrm{ne} - 1.23\ \mathrm{V} \quad (5)$$

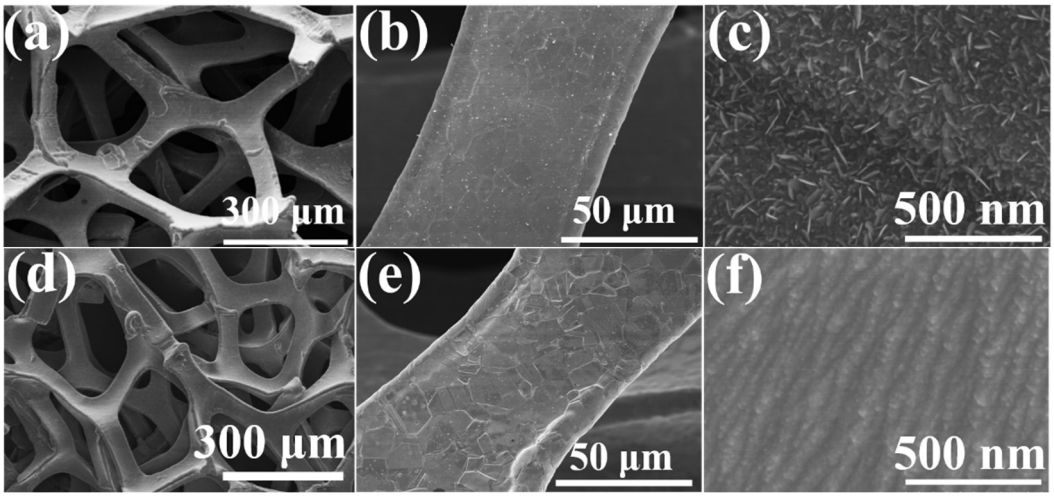

Figure S1. (a-c) SEM images of the APPJ-Ni_xO_y/NF-5 obtained from 5 min of the APPJ treatment time. (d-f) SEM images of the pristine NF.

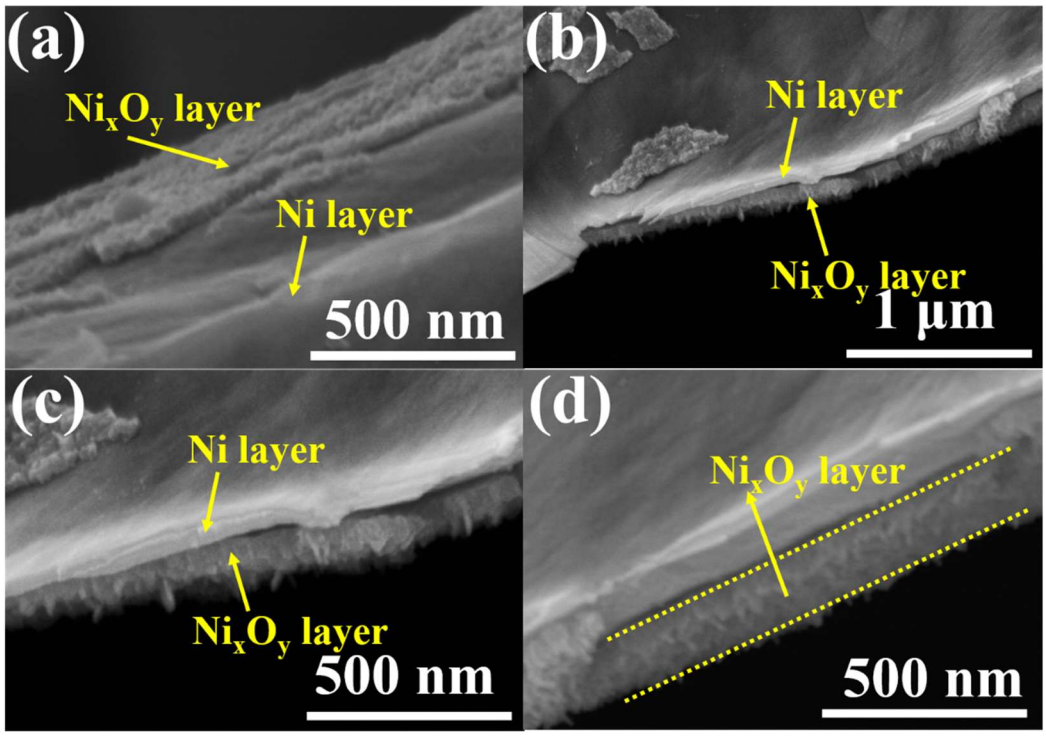

Figure S2. (a) Surface SEM image and (b-d) Cross-section SEM images of the APPJ-Ni_xO_y/NFs.

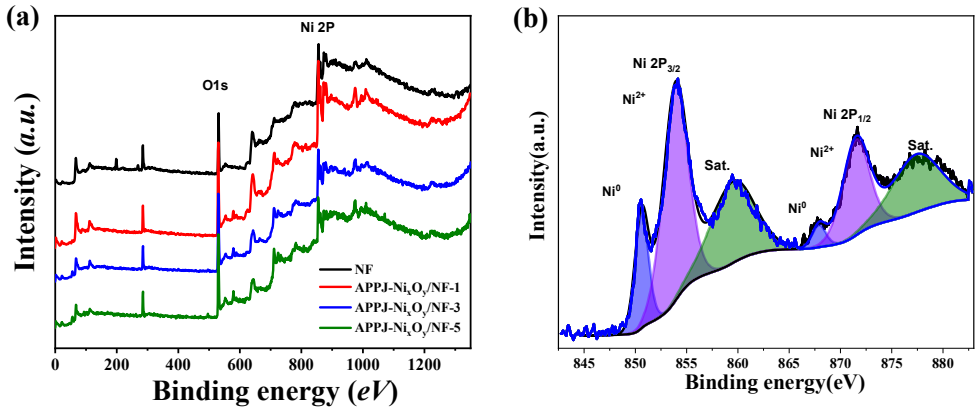

Figure S3. (a) XPS survey spectra of the pristine NF and the APPJ-Ni_xO_y/NFs with different durations of the APPJ treatment. (b) High-resolution XPS spectra of Ni 2p of the pristine NF.

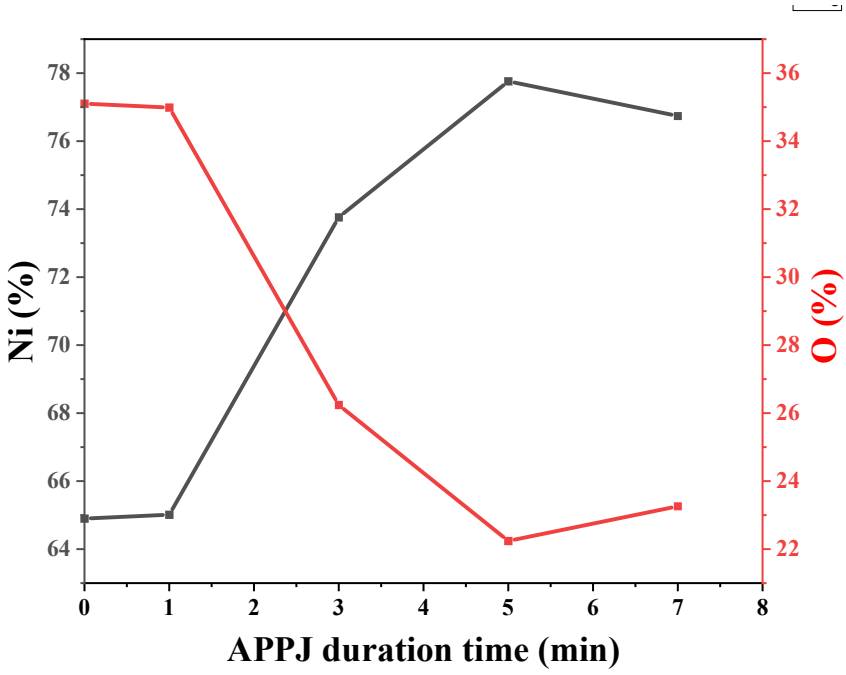

Figure S4. Changes of Ni and oxygen content with different durations of the APPJ treatment.

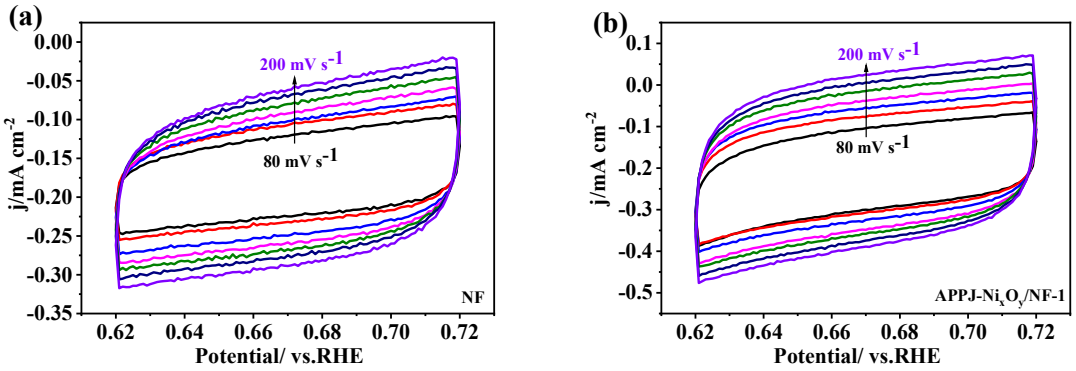

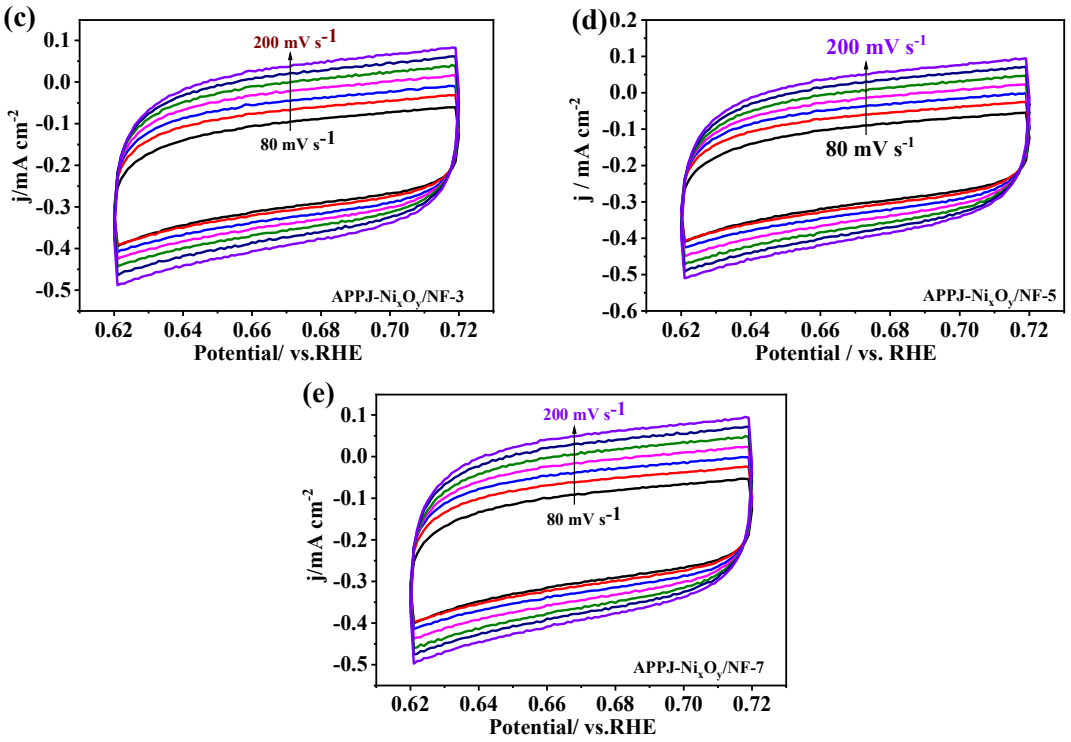

Figure S5. CVs recorded at various scan rates for (a) NF, (b) APPJ-Ni_xO_y/NF-1, (c) APPJ-Ni_xO_y/NF-3, (d) APPJ-Ni_xO_y/NF-5, and (e) APPJ-Ni_xO_y/NF-7.

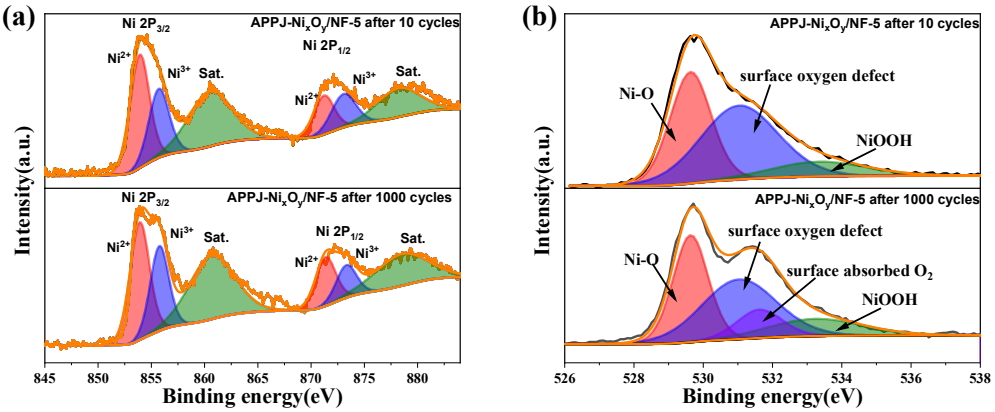

Figure S6. High-resolution XPS spectra of (a) Ni 2p and (b) O 1s for the APPJ-Ni_xO_y/NF-5 after 10 and 1000 cycles of the CV scans, respectively.

Table S1. Comparison of the OER performance of the APPJ-Ni_xO_y/NFs with different durations of the APPJ treatment.

Catalysts	E_{onset} **(V vs RHE)**	**η_{10} (mV vs RHE)**	$j_{\eta=400mV}$ **(mAcm^{-2})**	**Tafel slop (mV dec^{-1})**	Charge transfer resistance (R_{ct}) (Ω)
the pristine NF	1.567	434	4.96	180	45.6
APPJ-	1.501	378	19.6	92	30.1

Ni_xO_y/NF-1					
APPJ-Ni_xO_y/NF-3	1.494	370	23.6	89	26.2
APPJ-Ni_xO_y/NF-5	1.490	355	37.7	88	17.1
APPJ-Ni_xO_y/NF-7	1.489	356	35	89	18.2

Table S2. Comparison of the OER performance of the APPJ-Ni_xO_y/NF-5 with other non-noble electrocatalysts reported recently.

Catalysts	Substrate[a]	Electrolyte	η_{10} (mV vs RHE)	Tafel slop (mV dec^{-1})	Reference
APPJ-Ni_xO_y/NF-5	NF	1.0 M KOH	355	88	This Work
NiO@NF-6	NF	1.0 M KOH	405	109	[6]
15-30nm NiO NPs	GC	0.1 M KOH	396	54	[7]
~40nm NiO NPs	GC	1.0 M KOH	427	117	[8]
$Ni_xCo_{3-x}O_4$ nanowires	NF	1.0 M KOH	337	75	[9]
N-MWCNT/NiO-Ni	GC	1.0 M KOH	400	80	[10]
CoOx-ZIF	GC	1.0 M KOH	318	70.3	[11]
N-CoOx/CNT	GC	0.1 M KOH	420	68	[12]
Ni_3S_2	NF	1.0 M KOH	312	111	[13]
$ZnCo_2O_4$	FTO	1.0 M KOH	390	46	[14]
NiCo LDH	CP	1.0 M KOH	367	40	[15]

[a] GC: Glassy Carbon; FTO: Fluorine-doped tin oxide; CP: Carbon paper.

Table S3. Comparison of the OER performance of the APPJ-Ni_xO_y/NF-5 with other non-noble electrocatalysts prepared by using different plasma processes.

Materials	Type of plasma[a]	Condition[b]	Reaction time	η_{10} (mV vs RHE)	Tafel slop (mV dec^{-1})	Reference
APPJ-Ni_xO_y/NF-5	O_2 APPJ	RT	5 min	355	88	This Work
$CoMoO_4$/CC	Ar APPJ	RT	120 s	314	51	[16]
Cu_2O/CuO	He/O_2 APPJ	350℃	5 min	535	128	[17]
NiCoP/NF	PH_3/He RF	250℃, 980mTorr	15 min	280	87	[1]
P-Mo-$Ni(OH)_2$	H_2/N_2 RF	RT, 60Pa	20 min	/	/	[18]
P-V-NiFe LDH	H_2 RF	40Pa, 400W	20 min	/	/	[19]
Co_3O_4	Ar RF	40Pa, 100W	120 s	300	68	[20]
N-CoO_x/CNT	N_2 RF	0.1Torr, 200W, 200℃	5 min	420	68	[21]
CoFe LDHs	H_2O DBD	RT	5 min	232	36	[22]
Co-PBA/NF	Air DBD	RT	2 h	274	53	[23]
Cu_2S/CF	Air DBD	60℃	1 min	290	101	[24]
Co NPs/C	CH_4/H_2	25Torr, 700W	10 min	270	56	[25]

Co-FeCo/N-G	MW plasma $CH_4/H_2/NH_3$	10Torr, 1kV	10 min	310	34	[26]
MO-CNP	MW plasma C_6H_6 SPP	25kHz, 1.2kV	12 min	/	/	[27]
Ni_2P/NF	Ar/H_2 glow discharge	250°C, 50Pa	1 h	/	/	[28]

[a] MW: microwave; SPP: solution plasma process; [b] RT: room temperature

References

(1) Liang, H.; Gandi, A. N.; Anjum, D. H.; Wang, X.; Schwingenschlögl, U.; Alshareef, H. N. Plasma-Assisted Synthesis of NiCoP for Efficient Overall Water Splitting. *Nano Lett.* **2016,** *16* (12), 7718-7725.

(2) Kresse, G.; Furthmüller, J. Efficient iterative schemes for ab initio total-energy calculations using a plane-wave basis set. *Phys. Rev. B* **1996,** *54* (16), 11169-11186.

(3) Blöchl, P. E. Projector augmented-wave method. *Phys. Rev. B* **1994,** *50* (24), 17953-17979.

(4) Payne, M. C.; Teter, M. P.; Allan, D. C.; Arias, T. A.; Joannopoulos, J. D. Iterative minimization techniques for ab initio total-energy calculations: molecular dynamics and conjugate gradients. *Rev. Mod. Phys.* **1992,** *64* (4), 1045-1097.

(5) Su, C.-Y.; Cheng, H.; Li, W.; Liu, Z.-Q.; Li, N.; Hou, Z.; Bai, F.-Q.; Zhang, H.-X.; Ma, T.-Y. Atomic Modulation of FeCo–Nitrogen–Carbon Bifunctional Oxygen Electrodes for Rechargeable and Flexible All-Solid-State Zinc–Air Battery. *Adv. Energy Mater.* **2017,** *7* (13), 1602420.

(6) Zheng, J.; Zhou, W.; Liu, T.; Liu, S.; Wang, C.; Guo, L. Homologous NiO//Ni_2P nanoarrays grown on nickel foams: a well matched electrode pair with high stability in overall water splitting. *Nanoscale* **2017,** *9* (13), 4409-4418.

(7) Liu, R.; Liang, F.; Zhou, W.; Yang, Y.; Zhu, Z. Calcium-doped lanthanum nickelate layered perovskite and nickel oxide nano-hybrid for highly efficient water oxidation. *Nano Energy* **2015,** *12*, 115-122.

(8) Zhu, C.; Wen, D.; Leubner, S.; Oschatz, M.; Liu, W.; Holzschuh, M.; Simon, F.; Kaskel, S.; Eychmüller, A. Nickel cobalt oxide hollow nanosponges as advanced electrocatalysts for the oxygen evolution reaction. *Chem. Commun.* **2015,** *51* (37), 7851-7854.

(9) Yan, X.; Li, K.; Lyu, L.; Song, F.; He, J.; Niu, D.; Liu, L.; Hu, X.; Chen, X. From Water Oxidation to Reduction: Transformation from $Ni_xCo_{3-x}O_4$ Nanowires to NiCo/$NiCoO_x$ Heterostructures. *ACS Appl. Mater. Interfaces* **2016,** *8* (5), 3208-3214.

(10) Liu, X.; Park, M.; Kim, M. G.; Gupta, S.; Wu, G.; Cho, J. Integrating NiCo Alloys with Their Oxides as Efficient Bifunctional Cathode Catalysts for Rechargeable Zinc–Air Batteries. *Angew. Chem. Int. Ed.* **2015,** *54* (33), 9654-9658.

(11) Dou, S.; Dong, C.-L.; Hu, Z.; Huang, Y.-C.; Chen, J.-l.; Tao, L.; Yan, D.; Chen, D.; Shen, S.; Chou, S.; Wang, S. Atomic-Scale CoO_x Species in Metal–Organic

Frameworks for Oxygen Evolution Reaction. *Adv. Funct. Mater.* **2017,** *27* (36), 1702546.
(12) Sun, X.; Yang, X.; Xiang, H.; Mi, H.; Zhang, P.; Ren, X.; Li, Y.; Li, X. Nitrogen-doped CoO_x/carbon nanotubes derived by plasma-enhanced atomic layer deposition: Efficient bifunctional electrocatalyst for oxygen reduction and evolution reactions. *Electrochim. Acta.* **2019,** *296*, 964-971.
(13) Ren, G.; Hao, Q.; Mao, J.; Liang, L.; Liu, H.; Liu, C.; Zhang, J. Ultrafast fabrication of nickel sulfide film on Ni foam for efficient overall water splitting. *Nanoscale* **2018,** *10* (36), 17347-17353.
(14) Kim, T. W.; Woo, M. A.; Regis, M.; Choi, K.-S. Electrochemical Synthesis of Spinel Type $ZnCo_2O_4$ Electrodes for Use as Oxygen Evolution Reaction Catalysts. *J. Phys. Chem. Lett.* **2014,** *5* (13), 2370-2374.
(15) Liang, H.; Meng, F.; Cabán-Acevedo, M.; Li, L.; Forticaux, A.; Xiu, L.; Wang, Z.; Jin, S. Hydrothermal Continuous Flow Synthesis and Exfoliation of NiCo Layered Double Hydroxide Nanosheets for Enhanced Oxygen Evolution Catalysis. *Nano Lett.* **2015,** *15* (2), 1421-1427.
(16) Jiang, H.; Cui, Z.; Xu, C.; Li, W. Humid atmospheric pressure plasma jets exposed micro-defects on $CoMoO_4$ nanosheets with enhanced OER performance. *Chem. Commun.* **2019,** *55* (64), 9432-9435.
(17) Dey, A.; Chandrabose, G.; Damptey, L. A. O.; Erakulan, E. S.; Thapa, R.; Zhuk, S.; Dalapati, G. K.; Ramakrishna, S.; Braithwaite, N. S. J.; Shirzadi, A.; Krishnamurthy, S. Cu_2O/CuO heterojunction catalysts through atmospheric pressure plasma induced defect passivation. *Appl. Surf. Sci.* **2021,** *541*, 148571.
(18) Zhang, W.; Tang, Y.; Yu, L.; Yu, X.-Y. Activating the alkaline hydrogen evolution performance of Mo-incorporated $Ni(OH)_2$ by plasma-induced heterostructure. *Appl. Catal. B-Environ.* **2020,** *260*, 118154.
(19) Tang, Y.; Liu, Q.; Dong, L.; Wu, H. B.; Yu, X.-Y. Activating the hydrogen evolution and overall water splitting performance of NiFe LDH by cation doping and plasma reduction. *Appl. Catal. B-Environ.* **2020,** *266*, 118627.
(20) Xu, L.; Jiang, Q.; Xiao, Z.; Li, X.; Huo, J.; Wang, S.; Dai, L. Plasma-Engraved Co_3O_4 Nanosheets with Oxygen Vacancies and High Surface Area for the Oxygen Evolution Reaction. *Angew. Chem. Int. Ed.* **2016,** *55* (17), 5277-5281.
(21) Sun, X.; Yang, X.; Xiang, H.; Mi, H.; Zhang, P.; Ren, X.; Li, Y.; Li, X. Nitrogen-doped CoO_x/carbon nanotubes derived by plasma-enhanced atomic layer deposition: Efficient bifunctional electrocatalyst for oxygen reduction and evolution reactions. *Electrochim. Acta* **2019,** *296*, 964-971.
(22) Liu, R.; Wang, Y.; Liu, D.; Zou, Y.; Wang, S. Water-Plasma-Enabled Exfoliation of Ultrathin Layered Double Hydroxide Nanosheets with Multivacancies for Water Oxidation. *Adv. Mater.* **2017,** *29* (30), 1701546.
(23) Guo, Y.; Wang, T.; Chen, J.; Zheng, J.; Li, X.; Ostrikov, K. Air Plasma Activation of Catalytic Sites in a Metal-Cyanide Framework for Efficient Oxygen Evolution Reaction. *Adv. Energy Mater.* **2018,** *8* (18), 1800085.
(24) Lee, D.-H.; Lee, B.-H.; Sinha, A. K.; Park, J.-H.; Kim, M.-S.; Park, J.; Shin, H.; Lee, K.-S.; Sung, Y.-E.; Hyeon, T. Engineering titanium dioxide nanostructures

for enhanced lithium-ion storage. *J. Am. Chem. Soc.* **2018,** *140*, 16676-16684.
(25) Jin, Q.; Ren, B.; Li, D.; Cui, H.; Wang, C. Plasma-Assisted Synthesis of Self-Supporting Porous CoNPs@C Nanosheet as Efficient and Stable Bifunctional Electrocatalysts for Overall Water Splitting. *ACS Appl. Mater. Interfaces* **2017,** *9* (37), 31913-31921.
(26) Jin, Q.; Ren, B.; Chen, J.; Cui, H.; Wang, C. A facile method to conduct 3D self-supporting Co-FeCo/N-doped graphene-like carbon bifunctional electrocatalysts for flexible solid-state zinc air battery. *Appl. Catal. B-Environ.* **2019,** *256*, 117887.
(27) Kim, H.-m.; Saito, N.; Kim, D.-w. Enhancing Bifunctional Catalytic Activity of Oxygen Reduction and Evolution Reaction via One-Pot Formation of MnO_2-Carbon Hybrid Nanocomposite. *ChemistrySelect* **2018,** *3* (23), 6302-6308.
(28) Wu, X.; Guo, Y.; Wang, T.; Sun, B.; Liu, Z.; Wu, Y.; Zhang, S.; Zheng, J.; Li, X. Plasma enabled non-thermal phosphorization for nickel phosphide hydrogen evolution catalysts. *Chem. Commun.* **2019,** *55* (29), 4202-4205.